

# Ensemble Riemannian Data Assimilation for High-dimensional Nonlinear Dynamics

Sagar Kumar Tamang<sup>1</sup>, Ardeshir M. Ebtehaj<sup>1</sup>, Peter Jan van Leeuwen<sup>2</sup>, Gilad Lerman<sup>1</sup>, and Efi Foufoula-Georgiou<sup>3</sup>

<sup>1</sup>University of Minnesota

<sup>2</sup>Colorado State University

<sup>3</sup>University of California, Irvine

November 22, 2022

## Abstract

This paper presents the results of an ensemble data assimilation methodology over the Wasserstein space for high-dimensional nonlinear dynamical systems, focusing on the chaotic Lorenz-96 model and a two-layer quasi-geostrophic model of atmospheric circulation. Unlike Euclidean data assimilation, this approach is equipped with a Riemannian geometry and formulates data assimilation as a Wasserstein barycenter between the forecast probability distribution and the normalized likelihood function. The methodology does not rely on any Gaussian assumptions and can intrinsically treat systematic model and observation errors. To cope with the computational cost of the Wasserstein distance, the paper examines the efficiency of the entropic regularization. Comparisons with the standard particle and stochastic ensemble Kalman filters demonstrate that under systematic errors the presented methodology could extend the forecast skills of nonlinear dynamical systems.

# Ensemble Riemannian Data Assimilation for High-dimensional Nonlinear Dynamics

Sagar K. Tamang<sup>1,2</sup>, Ardeshir Ebtehaj<sup>1,2</sup>, Peter J. van Leeuwen<sup>3</sup>, Gilad Lerman<sup>4</sup>, Efi  
Foufoula-Georgiou<sup>5,6</sup>

<sup>1</sup>St. Anthony Falls Laboratory, University of Minnesota-Twin Cities, Minnesota, USA

<sup>2</sup>Department of Civil, Environmental and Geo- Engineering, University of Minnesota-Twin  
Cities, Minnesota, USA

<sup>3</sup>Department of Atmospheric Science, Colorado State University, Fort Collins, Colorado,  
USA

<sup>4</sup>School of Mathematics, University of Minnesota-Twin Cities, Minnesota, USA

<sup>5</sup>Department of Civil and Environmental Engineering, University of California Irvine,  
Irvine, California, USA

<sup>6</sup>Department of Earth System Science, University of California Irvine, Irvine, California,  
USA

## Key Points:

- An ensemble data assimilation methodology based on the Wasserstein distance is presented for treating systematic errors in high-dimensional systems.
- The proposed methodology does not require any *a priori* assumption about the shape of the probability distributions.
- To reduce the computational cost, the methodology relies on entropic regularization.

## Abstract

This paper presents the results of an ensemble data assimilation methodology over the Wasserstein space for high-dimensional nonlinear dynamical systems, focusing on the chaotic Lorenz-96 model and a two-layer quasi-geostrophic model of atmospheric circulation. Unlike Euclidean data assimilation, this approach is equipped with a Riemannian geometry and formulates data assimilation as a Wasserstein barycenter between the forecast probability distribution and the normalized likelihood function. The methodology does not rely on any Gaussian assumptions and can intrinsically treat systematic model and observation errors. To cope with the computational cost of the Wasserstein distance, the paper examines the efficiency of the entropic regularization. Comparisons with the standard particle and stochastic ensemble Kalman filters demonstrate that under systematic errors the presented methodology could extend the forecast skills of nonlinear dynamical systems.

## 1 Introduction

The science of data assimilation (DA) aims to optimally combine the information content of observations with forecasts of Earth system models (ESM) to improve the estimation of their initial conditions and thus their predictive capabilities (Kalnay, 2003). Current DA methodologies, either variational (Courtier et al., 1994; A. C. Lorenc, 1986; Poterjoy & Zhang, 2014; Rabier et al., 2000; Zupanski, 1993) or filtering (J. Anderson & Lei, 2013; J. L. Anderson, 2001; Bishop et al., 2001; Janjić et al., 2011; Kalman, 1960; Lei et al., 2018; Tippett et al., 2003), largely rely on penalization of second-order statistics of the unbiased model and observation errors over the Euclidean space. For example, in the three-dimensional variational (3D-Var) DA (Courtier et al., 1998; Z. Li et al., 2013; A. Lorenc et al., 2000; A. C. Lorenc, 1986), a least-squares cost function comprising of weighted Euclidean distances of the state from the previous model forecasts (background state) and the observations is formulated. Solution of this cost function leads to an analysis state, which is a weighted average of the forecasts and observations across multiple dimensions of the problem with the weights dictated by prescribed background and observation error covariance matrices. The variants of the Kalman filtering DA methods (Evensen, 1994a, 2003; Houtekamer & Zhang, 2016; Nerger et al., 2012b; Reichle et al., 2002) also follow the same principle but in these methods, the background covariance contains information from past observations and model evolution.

Apart from the Euclidean distance, other measures and distance metrics including the quadratic mutual information (Kapur, 1994), Kullback-Leibler (KL) divergence (Kullback & Leibler, 1951), Hellinger distance (Hellinger, 1909), and Wasserstein distance (Villani, 2003) have been also utilized in DA frameworks. Among others, Tagade & Ravela (2014) introduced a nonlinear filter, where the analysis is obtained through maximization of the quadratic mutual information. Maclean et al. (2017) utilized the Hellinger distance to measure the difference between the predicted and observed spatial patterns in oceanic flows. Chianese et al. (2018) introduced a variational DA method in which minimization of the KL divergence led to an approximation of the bias terms and model parameters. Similarly, R. Li et al. (2019) employed the KL divergence in an optimization framework to incorporate inequality constraints in the Ensemble Kalman Filter (EnKF, Evensen, 1994b). Recently, Pulido & van

65 Leeuwen (2019) developed a mapping particle filter in which particles are pushed towards  
66 the posterior density by minimizing the KL divergence between the posterior and a series of  
67 intermediate probability densities.

68 In recent years, the Wasserstein or the Earth mover’s distance, originating from the the-  
69 ory of optimal mass transport (OMT, B. Chen et al., 2019; Y. Chen et al., 2017, 2018a,b;  
70 Kantorovich, 1942; Kolouri et al., 2017; Monge, 1781; Villani, 2003), has been gaining at-  
71 tention in the DA community. Reich (2013) first introduced a new resampling approach  
72 in particle filters using the OMT, to maximize the correlation between prior and posterior  
73 ensemble members. Ning et al. (2014) further utilized the Wasserstein distance to treat po-  
74 sition errors arising from uncertain model parameters. Following on this work, Feyeux et al.  
75 (2018) proposed to replace the weighted Euclidean distance with the Wasserstein distance in  
76 variational DA frameworks to treat position error. Tamang et al. (2020) proposed to use the  
77 Wasserstein distance to regularize a variational DA framework for treating systematic errors  
78 arising from the model forecast in chaotic systems. However, DA frameworks utilizing the  
79 Wasserstein distance are computationally expensive as they require obtaining a joint distri-  
80 bution that couples two marginal distributions. Finding this joint distribution often relies  
81 on interior-point methods (Altman & Gondzio, 1999) or the Orlin’s algorithm (Orlin, 1993)  
82 that have super-cubic run time – making the Wasserstein DA computationally challenging  
83 for high-dimensional geophysical problems. More recently, to reduce the computational cost,  
84 Tamang et al. (2021) used entropic regularization of the OMT formulation (Cuturi, 2013)  
85 through a new framework, called Ensemble Riemannian Data Assimilation (EnRDA) to cope  
86 with systematic biases.

87 In this paper, we expand EnRDA by testing and documenting its performance over “high-  
88 dimensional” nonlinear dynamical systems under systematic errors. Unlike Euclidean DA  
89 with a known connection with the family of Gaussian distributions through Bayes’ theorem,  
90 the EnRDA does not rely on any parametric assumptions about the input probability distri-  
91 butions. Therefore, it does not guarantee an analysis state with a minimum mean squared  
92 error. However, as it will be clear later on, it enables to optimally (i) interpolate between  
93 the forecast distribution and the normalized likelihood function without any parametric as-  
94 sumptions about their shapes and (ii) formally penalize systematic translations between  
95 them arising due to geophysical biases.

96 The paper poses the hypothesis that under geophysical biases and high-dimensional non-  
97 linear dynamical systems, EnRDA can lead to an analysis state with reduced uncertainty  
98 – compared to classic “unbiased” minimum mean-squared error Euclidean DA techniques.  
99 To test this hypothesis, we implement EnRDA on the chaotic Lorenz-96 system (Lorenz,  
100 1995) and a two-layer quasi-geostrophic (QG) model (Pedlosky et al., 1987). The results  
101 demonstrate that DA over the Wasserstein space provides an alternative approach that may  
102 enhance high-dimensional geophysical forecast skills when the distributions of the state vari-  
103 ables are not necessarily Gaussian and are corrupted with systematic errors.

104 The outline of the paper is as follows. Section 2 provides a brief background on optimal  
105 mass transport and Wasserstein distance. The EnRDA methodology is presented in Section  
106 3. Section 4 presents different test cases of implementation on the Lorenz-96 and the QG  
107 model and documents the performance of the presented approach in comparison with the  
108 classic implementation of the standard particle filter with resampling and the Stochastic  
109 Ensemble Kalman Filter (SEnKF). A summary and concluding remarks are presented in

110 Section 5. The details of the entropic regularization for the EnRDA, and covariance inflation  
 111 and localization procedures for the SEnKF are provided in Appendix A.

## 112 2 Background on OMT and the Wasserstein Barycen- 113 ters

114 We provide a brief background on the theory of optimal mass transport (OMT) and Wasser-  
 115 stein barycenters. The OMT theory, first put forward by Monge (1781), aims to find the  
 116 minimum cost of transporting distributed masses of materials from known source points to  
 117 target points. The theory was later expanded as a new tool to compare probability distri-  
 118 butions (Brenier, 1987; Villani, 2003) and since then has found its applications in the field  
 119 of data assimilation (Feyeux et al., 2018; L. Li et al., 2018; Ning et al., 2014; Tamang et al.,  
 120 2020), subsurface geophysical inverse problems (J. Chen et al., 2018; Yang & Engquist, 2018;  
 121 Yang et al., 2018; Yong et al., 2019) and comparisons of climate model simulations (Vissio  
 122 et al., 2020).

123 Let us consider a discrete source probability distribution  $p(\mathbf{x}) = \sum_{i=1}^M p_{\mathbf{x}_i} \delta_{\mathbf{x}_i}$  and a tar-  
 124 get distribution  $p(\mathbf{y}) = \sum_{j=1}^N p_{\mathbf{y}_j} \delta_{\mathbf{y}_j}$  with their respective probability masses  $\{\mathbf{p}_x \in \mathbb{R}_+^M : \sum_i p_{\mathbf{x}_i} = 1\}$   
 125 and  $\{\mathbf{p}_y \in \mathbb{R}_+^N : \sum_j p_{\mathbf{y}_j} = 1\}$  supported on  $m$ - and  $n$ -element column vectors  
 126  $\mathbf{x}_i \in \mathbb{R}^m$  and  $\mathbf{y}_j \in \mathbb{R}^n$ , respectively. The notation  $\mathbf{p}_x \in \mathbb{R}_+^M$  represents probability masses  $\mathbf{p}_x$   
 127 containing non-negative real numbers supported on  $M$  points, whereas  $\delta_{\mathbf{x}}$  is the Dirac func-  
 128 tion at  $\mathbf{x}$ . In the Monge formulation, the goal is to seek an optimal surjective transportation  
 129 map  $T_{\#}^a p(\mathbf{x}) = p(\mathbf{y})$  that “pushes forward” the source distribution  $p(\mathbf{x})$  towards the target  
 130 distribution  $p(\mathbf{y})$ , with a minimum transportation cost as follows:

$$T^a = \underset{T}{\operatorname{argmin}} \sum_{i=1}^M c(\mathbf{x}_i, T(\mathbf{x}_i)) \quad \text{s.t.} \quad T_{\#}^a p(\mathbf{x}) = p(\mathbf{y}), \quad (1)$$

131 where  $c(\cdot, \cdot) \in \mathbb{R}_+$  represents the cost of transporting a unit mass from one support point in  
 132  $\mathbf{x}$  to another one in  $\mathbf{y}$ .

133 The problem formulation by Monge as expressed in Equation 1, however, is non-convex  
 134 and the existence of an optimal transportation map is not guaranteed (Y. Chen et al., 2019)  
 135 – especially, when the number of support points for the target distribution exceeds that of  
 136 the source distribution ( $N > M$ ) (Peyré et al., 2019). This limitation was overcome by  
 137 Kantorovich (1942) who introduced a probabilistic formulation of OMT – allowing splitting  
 138 of probability mass from a single source point to multiple target points. The Kantorovich  
 139 formalism recasts the OMT problem in a linear programming framework that finds an opti-  
 140 mal joint distribution or coupling  $\mathbf{U}^a \in \mathbb{R}_+^{M \times N}$  that couples the marginal source and target  
 141 distributions with the following optimality criterion:

$$\mathbf{U}^a = \underset{\mathbf{U}}{\operatorname{argmin}} \operatorname{tr}(\mathbf{C}^T \mathbf{U}) \quad \text{s.t.} \quad \begin{cases} \mathbf{U} \in \mathbb{R}_+^{M \times N} \\ \mathbf{U} \mathbf{1}_N = \mathbf{p}_x \\ \mathbf{U}^T \mathbf{1}_M = \mathbf{p}_y \end{cases}, \quad (2)$$

142 where  $\text{tr}(\cdot)$  is the trace of a matrix,  $(\cdot)^T$  is the transposition operator and  $\mathbb{1}_M$  represents an  
 143  $M$ -element column vector of ones. In the above formulation, the known  $\{\mathbf{C} \in \mathbb{R}_+^{M \times N} : c_{ij} =$   
 144  $\|\mathbf{x}_i - \mathbf{y}_j\|_2^2\}$  denotes the so-called transportation cost matrix which is defined based on the  
 145  $\ell_2$ -norm  $\|\cdot\|_2$  or the Euclidean distance between the support points of the source and target  
 146 distributions. Here, the  $(i, j)^{\text{th}}$  element  $u_{ij}^a$  of optimal joint distribution  $\mathbf{U}^a$  represents the  
 147 respective amount of mass transported from support point  $\mathbf{x}_i$  to  $\mathbf{y}_j$ . Then, the 2-Wasserstein  
 148 distance or metric between the marginal probability distributions is defined as the square  
 149 root of the optimal transportation cost  $d_{\mathcal{W}}(\mathbf{p}_x, \mathbf{p}_y) = (\text{tr}(\mathbf{C}^T \mathbf{U}^a))^{\frac{1}{2}}$  (Dobrushin, 1970; Villani,  
 150 2008). It should be noted that due to the linear equality and non-negativity constraints in  
 151 Equation 2, the family of joint distributions that satisfy these constraints forms a bounded  
 152 convex polytope (Cuturi & Peyré, 2018) and consequently, the optimal joint distribution  $\mathbf{U}^a$   
 153 is located on one of the extreme points of such a polytope (Peyré et al., 2019).

154 Recalling that over the Euclidean space, the barycenter of a group of points is equivalent  
 155 to their (weighted) mean value. The Wasserstein metric offers a Riemannian generalization  
 156 of this problem and allows to define the barycenter of a family of probability distributions  
 157 (Bigot et al., 2012; Rabin et al., 2011; Srivastava et al., 2018). In particular, for a group  
 158 of  $K$  probability mass functions  $\mathbf{p}_1, \dots, \mathbf{p}_K$ , a Wasserstein barycenter  $\mathbf{p}_\eta$  is defined as their  
 159 Fréchet mean (Fréchet, 1948) as follows (Agueh & Carlier, 2011):

$$\mathbf{p}_\eta = \underset{\mathbf{p}}{\text{argmin}} \sum_{k=1}^K \eta_k d_{\mathcal{W}}^2(\mathbf{p}, \mathbf{p}_k), \quad (3)$$

160 where  $\{(\eta_1, \dots, \eta_K)^T \in \mathbb{R}_+^K : \sum_k \eta_k = 1\}$  represent the weights associated with  
 161 the respective distributions. In special cases where the group of  $K$  distributions is  
 162 Gaussian  $\{\mathcal{N}(\boldsymbol{\mu}_1, \boldsymbol{\Sigma}_1), \dots, \mathcal{N}(\boldsymbol{\mu}_K, \boldsymbol{\Sigma}_K)\}$  with mean  $\boldsymbol{\mu}_1, \dots, \boldsymbol{\mu}_K$  and positive definite co-  
 163 variance  $\boldsymbol{\Sigma}_1, \dots, \boldsymbol{\Sigma}_K$ , the Wasserstein barycenter is also a Gaussian density  $\mathcal{N}(\boldsymbol{\mu}_\eta, \boldsymbol{\Sigma}_\eta)$   
 164 with  $\boldsymbol{\mu}_\eta = \sum_k \eta_k \boldsymbol{\mu}_k$  and  $\boldsymbol{\Sigma}_\eta$  is the unique positive definite root of the matrix equation  
 165  $\boldsymbol{\Sigma} = \sum_k \eta_k (\boldsymbol{\Sigma}^{\frac{1}{2}} \boldsymbol{\Sigma}_k \boldsymbol{\Sigma}^{\frac{1}{2}})^{\frac{1}{2}}$  (Agueh & Carlier, 2011).

### 166 3 Ensemble Riemannian Data Assimilation (EnRDA)

167 Let us assume that the evolution of the  $i^{\text{th}}$  ensemble member  $\mathbf{x}_i \in \mathbb{R}^m$  of ESM simulations  
 168 can be presented as the following stochastic dynamical system:

$$\mathbf{x}_i^t = \mathcal{M}(\mathbf{x}_i^{t-1}) + \boldsymbol{\omega}_i^t \quad i = 1, \dots, M, \quad (4)$$

169 where  $\mathcal{M} : \mathbb{R}^m \rightarrow \mathbb{R}^m$  is the deterministic nonlinear model operator, evolving the model  
 170 state in time with a stochastic error term  $\boldsymbol{\omega}_i^t \in \mathbb{R}^m$ . This dynamical system is observed at  
 171 time  $t$  through an observation equation  $\mathbf{y}^t = \mathcal{H}(\mathbf{x}^t) + \mathbf{v}^t$ , where  $\mathcal{H} : \mathbb{R}^m \rightarrow \mathbb{R}^n$  maps the  
 172 state to the observation space and  $\mathbf{v}^t \in \mathbb{R}^n$  represents an additive observation error. Note  
 173 that the error terms are not necessarily drawn from Gaussian distributions but need to have  
 174 finite second-order moments.

175 Hereafter, we drop the time superscript for brevity and represent the model (or back-  
 176 ground) probability distribution as  $p(\mathbf{x}) = \sum_{i=1}^M p_{\mathbf{x}_i} \delta_{\mathbf{x}_i}$  with its probability mass vector  
 177  $\{\mathbf{p}_x \in \mathbb{R}_+^M : \sum_i p_{\mathbf{x}_i} = 1\}$ . Furthermore, the normalized likelihood function is repre-  
 178 sented as  $\tilde{p}(\mathbf{y}|\mathbf{x})$  centered at the given observation  $\mathbf{y}$  with its probability mass vector  
 179  $\{\tilde{\mathbf{p}}_{y|x} \in \mathbb{R}_+^N : \sum_j \tilde{p}_{y|x_j} = 1\}$ . The probability distribution of the analysis state  $p(\mathbf{x}_a)$ , is  
 180 then defined as the Wasserstein barycenter between forecast distribution and the normalized  
 181 likelihood function:

$$p(\mathbf{x}_a) = \operatorname{argmin}_{p(\mathbf{z})} \left\{ \eta d_{\mathcal{W}}^2[p(\mathbf{x}), p(\mathbf{z})] + (1 - \eta) d_{\mathcal{W}}^2[\tilde{p}(\mathbf{y}|\mathbf{x}), p(\mathbf{z})] \right\}, \quad (5)$$

182 where  $\eta \in [0, 1]$  is a displacement parameter that controls the relative weight of the back-  
 183 ground and observation. The displacement parameter  $\eta$  is a hyperparameter that captures  
 184 the relative weights of the histogram of the background state and likelihood function in char-  
 185 acterization of the analysis state distribution as a Wasserstein barycenter. The optimal value  
 186 of  $\eta$  needs to be determined offline, using reference data through cross-validation studies. It  
 187 is important to note that the above formalism requires all dimensions to be observable and  
 188 thus those dimensions with no observations cannot be updated, which is a limitation of the  
 189 current formalism compared to the Euclidean DA. This limitation is further discussed later  
 190 on in Section 5.

191 To solve the above DA problem, we need to characterize the background distribution and  
 192 the normalized likelihood function. Similar to the approach used in particle filter (Gordon et  
 193 al., 1993; van Leeuwen, 2010), we suggest approximating them through ensemble realizations.  
 194 For constructing the histogram of the normalized likelihood function, we can draw  $N$  samples  
 195 at each assimilation cycle by perturbing the available observation  $\mathbf{y}$  with the observation error  
 196  $\mathcal{N}(0, \mathbf{R})$ .

197 To obtain the Wasserstein barycenter  $p(\mathbf{x}_a)$  in Equation 5, we use the McCann’s formalism  
 198 (McCann, 1997; Peyré et al., 2019):

$$p(\mathbf{x}_a) = \sum_{i=1}^M \sum_{j=1}^N u_{ij}^a \delta_{\mathbf{z}_{ij}}, \quad (6)$$

199 where  $\mathbf{z}_{ij} = \eta \mathbf{x}_i + (1 - \eta) \mathbf{y}_j$  represents the support points of the analysis distribution and  
 200  $u_{ij}^a$  are the elements of the joint distribution  $\{\mathbf{U}^a \in \mathbb{R}_+^{M \times N} : \sum_i \sum_j u_{ij} = 1\}$ . It is important  
 201 to note that the analysis state histogram, at each assimilation cycle, is supported on at most  
 202  $M + N - 1$  points, which is the maximum number of non-zero entries in the optimal joint  
 203 coupling (Peyré et al., 2019). To keep the number of ensemble members constant throughout,  
 204  $M$  ensemble members are resampled from  $p(\mathbf{x}_a)$  using the multinomial resampling scheme  
 205 (T. Li et al., 2015).

206 Computation of the joint distribution in Equation 2 is computationally expensive as  
 207 explained previously and can be prohibitive for high-dimensional geophysical problems. As  
 208 suggested by Cuturi (2013), to reduce the computational cost, we regularize the cost function  
 209 in the optimal transportation plan formulation of EnRDA by a Gibbs-Boltzmann entropy

210 function:

$$\mathbf{U}^a = \underset{\mathbf{U}}{\operatorname{argmin}} \operatorname{tr}(\mathbf{C}^T \mathbf{U}) - \gamma \operatorname{tr}(\mathbf{U}^T [\log(\mathbf{U} - \mathbb{1}_M \mathbb{1}_N^T)]) \quad \text{s.t.} \quad \begin{cases} \mathbf{U} \in \mathbb{R}_+^{M \times N} \\ \mathbf{U} \mathbb{1}_N = \mathbf{p}_x \\ \mathbf{U}^T \mathbb{1}_M = \tilde{\mathbf{p}}_{y|x} \end{cases}, \quad (7)$$

211 where  $\gamma \in \mathbb{R}_+$  is a regularization parameter. The entropic regularization transforms the  
 212 original OMT formulation to a strictly convex problem, which can then be efficiently solved  
 213 using Sinkhorn’s algorithm (Sinkhorn, 1967). The details of Sinkhorn’s algorithm for solving  
 214 regularized optimal transportation problems are presented in Appendix A.1. The regular-  
 215 ization parameter  $\gamma$  balances the solution between the optimal joint distribution and the one  
 216 that maximizes the relative entropy. It is evident from Equation 7 that at the limit  $\gamma \rightarrow 0$ ,  
 217 the solution of Equation 7 converges to the analysis joint distribution with a minimum mor-  
 218 phing cost. However, as the value of  $\gamma$  increases, the convexity of the problem also increases,  
 219 enabling the deployment of more efficient optimization algorithms than classic solvers of  
 220 linear programming problems (Dantzig et al., 1955; Orlin, 1993). At the same time, the  
 221 number of non-zero entries of the joint coupling increases from  $M + N - 1$  to  $MN$  points as  
 222  $\gamma \rightarrow \infty$ , which results in a maximum entropy solution that converges to  $\mathbf{U}^a \rightarrow \mathbf{p}_x \tilde{\mathbf{p}}_{y|x}^T$ . For  
 223 a more comprehensive explanation of EnRDA, one can refer to Tamang et al. (2021).

224 As an example, we examine here the solution of Equation 5 between a banana-shaped  
 225 distribution denoted by  $\mathcal{F}(\xi_1, \xi_2, \xi_3, b) \propto \exp(-\xi_1(4 - b x_1 - x_2^2) - \xi_2(x_1^2 - \xi_3 x_2^2))$  and a  
 226 bivariate Gaussian distribution as a function of the displacement parameter  $\eta \in [0, 1]$  –  
 227 resembling the background distribution  $p(\mathbf{x})$  and the normalized likelihood function  $\tilde{p}(\mathbf{y}|\mathbf{x})$ ,  
 228 respectively with regularization parameter  $\gamma = 1000$ . As seen from Figure 1, for lower values  
 229 of  $\eta$ , the analysis state distribution is closer to the observation and its shape resembles the  
 230 Gaussian distribution. However, as the value of  $\eta$  increases, the analysis state distribution  
 231 moves closer to the background distribution and starts morphing into a banana-shaped  
 232 distribution. Therefore, the analysis state distribution is defined as the one that is sufficiently  
 233 close to the background distribution and the normalized likelihood function not only based  
 234 on their shape but also their central location – depending on the displacement parameter.  
 235 Thus, unlike the Euclidean barycenter, this approach does not guarantee that the mean  
 236 or mode of the analysis state probability distribution is a minimum mean-squared error  
 237 estimate of the initial condition. In the next section, we present results from systems of well-  
 238 known dynamics to test the main hypothesis of the paper, that is, to investigate whether  
 239 EnRDA can lead to an improved approximation of the analysis state under systematic error  
 240 in high-dimensional nonlinear dynamics, where the distribution of the background state is  
 241 not necessarily Gaussian.

## 242 4 Numerical Experiments and Results

### 243 4.1 Lorenz-96

244 The Lorenz model (Lorenz-96, Lorenz, 1995), which is widely adopted as a testbed for  
 245 numerous DA experiments (Lguensat et al., 2017; Shen & Tang, 2015; Tang et al., 2014; Tian  
 246 et al., 2018; Trevisan & Palatella, 2011), offers a simplified representation of the extra-tropical

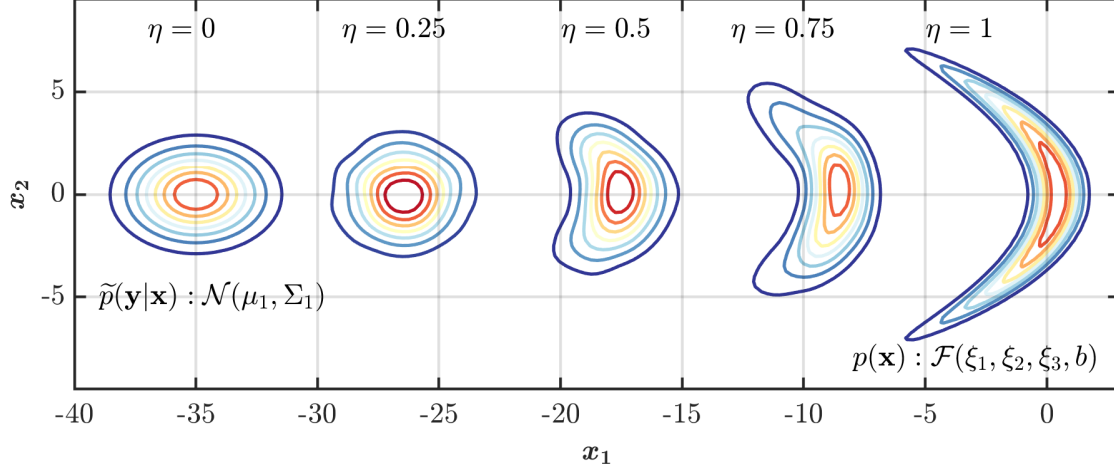


Figure 1: The analysis distribution obtained as a Wasserstein barycenter for different values of the displacement parameter  $\eta \in [0, 1]$  between a background distribution represented by a banana-shaped distribution  $p(\mathbf{x}) : \mathcal{F}(\xi_1, \xi_2, \xi_3, b)$  with  $\xi_1 = 0.02$ ,  $\xi_2 = 0.06$ ,  $\xi_3 = 1.6$ , and  $b = 8$ , and the normalized likelihood function represented by a bivariate Gaussian  $\tilde{p}(\mathbf{y}|\mathbf{x}) : \mathcal{N}(\boldsymbol{\mu}_1, \boldsymbol{\Sigma}_1)$ , where  $\boldsymbol{\mu}_1 = \begin{bmatrix} -35 \\ 0 \end{bmatrix}$  and  $\boldsymbol{\Sigma}_1 = \begin{bmatrix} 3 & 0 \\ 0 & 2 \end{bmatrix}$ .

247 dynamics in the Earth’s atmosphere. The model coordinates  $\{\mathbf{x} = (x_1, \dots, x_K)^T \in \mathbb{R}^K\}$  at  
 248  $K$  dimensions represent the state of an arbitrary atmospheric quantity measured along the  
 249 Earth’s latitudes at  $K$  equally spaced longitudinal slices. The model is designed to mimic  
 250 the continuous-time variation in atmospheric quantities due to interactions between three  
 251 major components namely advection, internal dissipation, and external forcing. The model  
 252 dynamics is represented as follows:

$$\frac{dx_k}{dt} = (x_{k+1} - x_{k-2})x_{k-1} - x_k + F, \quad k = 1, \dots, K, \quad (8)$$

253 where  $F \in \mathbb{R}_+$  is a constant external forcing independent of the model state. The Lorenz-96  
 254 model has cyclic boundaries with  $x_{-1} = x_{K-1}$ ,  $x_0 = x_K$ , and  $x_{K+1} = x_1$ . It is known that for  
 255 small values of  $F < 8/9$ , the system approaches a steady state condition with each coordinate  
 256 value converging to the external forcing  $x_k \rightarrow F$ ,  $\forall k$ , whereas for  $F > 8/9$ , chaos develops  
 257 (Lorenz & Emanuel, 1998). For standard model setup with  $F = 8$ , the system is known to  
 258 exhibit highly chaotic behavior with the largest Lyapunov exponent of 1.67 (Brajard et al.,  
 259 2020).

#### 260 4.1.1 Experimental Setup, Results and Discussion

261 We focus on the 40-dimensional Lorenz-96 system (i.e.  $K = 40$ ) and compare EnRDA results  
 262 with the classic implementation of the particle filter (PF, Gordon et al., 1993; Poterjoy & An-  
 263 derson, 2016; Van Leeuwen, 2009; van Leeuwen, 2010) and the Stochastic Ensemble Kalman  
 264 filter (SEnKF, J. L. Anderson, 2016; Burgers et al., 1998; Evensen, 1994b; Houtekamer &  
 265 Mitchell, 1998; Janjić et al., 2011; Van Leeuwen, 2020). Similar to the experimental set-  
 266 ting suggested in (Lorenz & Emanuel, 1998; Nerger et al., 2012a), we initialize the model by

267 choosing  $x_{20} = 8.008$  and  $x_k = 8$  for all other model coordinates. In order to avoid any initial  
 268 transient effect, the model in Equation 8 is integrated for 1000 time steps using the fourth-  
 269 order Runge-Kutta approximation (Kutta, 1901; Runge, 1895) with a non-dimensional time  
 270 step of  $\Delta t = 0.01$  and the endpoint of the run is utilized as the initial condition for DA  
 271 experimentation.

272 Similar to the suggested experimental setting in (van Leeuwen, 2010), we obtain the  
 273 ground truth by integrating Equation 8 with a time step of  $\Delta t$  over a time period of  $T =$   
 274  $0-20$  in the absence of any model error. The observations are assumed to be available at  
 275 each assimilation time interval of  $10\Delta t$  and deviated from the ground truth by a Gaussian  
 276 error  $\mathbf{v}_t \sim \mathcal{N}(0, \sigma_{\text{obs}}^2 \Sigma_\rho)$ , with  $\sigma_{\text{obs}}^2 = 1$  and the correlation matrix  $\Sigma_\rho \in \mathbb{R}_+^{40 \times 40}$  with 1 on the  
 277 diagonals, 0.5 on the first sub- and super-diagonals, and 0 everywhere else. The observation  
 278 time step of  $10\Delta t$  is equivalent to 12 hours in global ESMs (Lorenz, 1995).

279 To characterize the distribution of the background state for each DA methodology, 50  
 280 (5000) ensemble members (particles) for the SEnKF and EnRDA (PF) are generated using  
 281 model errors  $\boldsymbol{\omega}_t \sim \mathcal{N}(0, \sigma_t^2 \mathbf{I}_{40})$  with  $\sigma_t^2 = 0.25$  for  $t > 0$  and  $\sigma_0^2 = 4$ , where throughout  $\mathbf{I}_m$   
 282 represents an  $m \times m$  identity matrix. To alleviate the known degeneracy problem in the  
 283 PF, a higher number of particles was used. Furthermore, to introduce additional systematic  
 284 background error, we utilize an erroneous external forcing of  $F_m = 6$  instead of the “true”  
 285 forcing value  $F = 8$ . To have a robust inference, the average values of the error metrics  
 286 are reported for 50 experiments using different random realizations. As will be elaborated  
 287 later on, we set the EnRDA displacement parameter  $\eta = 0.44$ , determined through a cross-  
 288 validation study based on a minimum mean-squared error criterion. This tuning is similar  
 289 to tuning inflation and localization parameters in a typical EnKF, or tuning length-scales in  
 290 3D- or 4D-Var. Note that we already introduced some systematic error because the truth  
 291 has zero model error, while the prior does have model errors. In a fully unbiased set up the  
 292 truth and the prior are drawn from the same distribution.

293 The results of EnRDA are shown in Figure 2. In the left panel, the temporal evolution of  
 294 the ground truth and EnRDA analysis state is shown over all dimensions of the Lorenz-96,  
 295 while a snapshot at time 10 [t] is presented in the right panel. The analysis state obtained  
 296 from EnRDA follows the ground truth reasonably well during all time steps with a root mean-  
 297 squared error (rmse) of 0.85. The comparison of EnRDA with the classic implementations  
 298 of the SEnKF and PF are shown in Figure 3 (a-c). It can be seen that the rmse of the  
 299 PF increases sharply over time, suggesting that the problem of filter degeneracy still exists  
 300 despite the higher number of particles. This problem is exacerbated due to the presence  
 301 of bias causing a rapid collapse of the ensemble variance over time as more particles fall  
 302 outside of the support set of the likelihood function. The root mean-squared error of both  
 303 the SEnKF and EnRDA is stabilized over time and is smaller by  $\sim 20\%$  (80%) in EnRDA  
 304 compared to the SEnKF (PF). It is important to note that the presence of systematic bias due  
 305 to erroneous choice of the external forcing inherently favors EnRDA over SEnKF since the  
 306 latter is a minimum variance unbiased estimator at the limit  $M \rightarrow \infty$ , where  $M$  represents  
 307 the number of ensemble members.

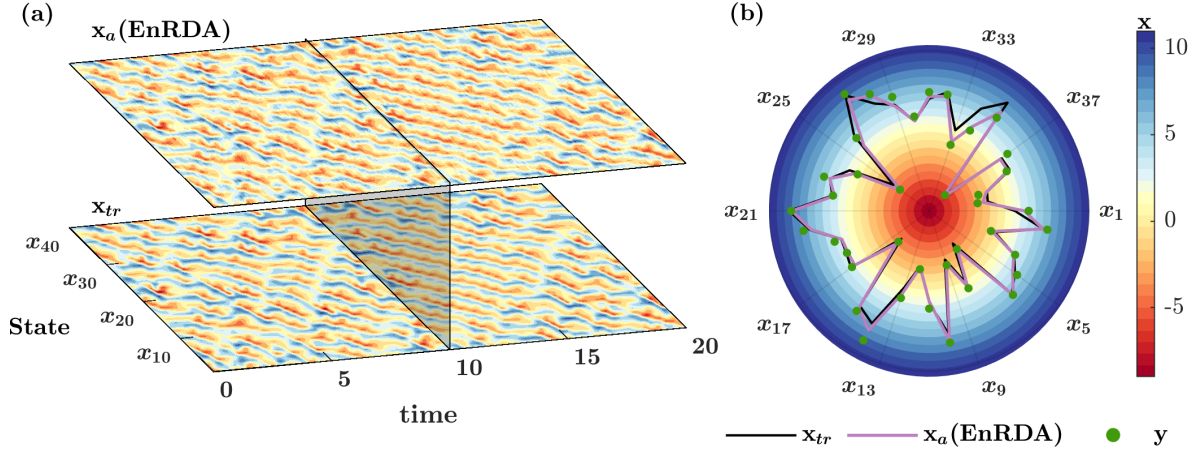


Figure 2: (a) Temporal evolution of the ground truth  $\mathbf{x}_{tr}$  and analysis state  $\mathbf{x}_a$  by ensemble Riemannian data assimilation (EnRDA) for  $K = 40$  dimensions of the Lorenz-96 over  $T = 0-20$  [t] and (b) their snapshots at  $T = 10$  [t] together with the available observations  $\mathbf{y}$ .

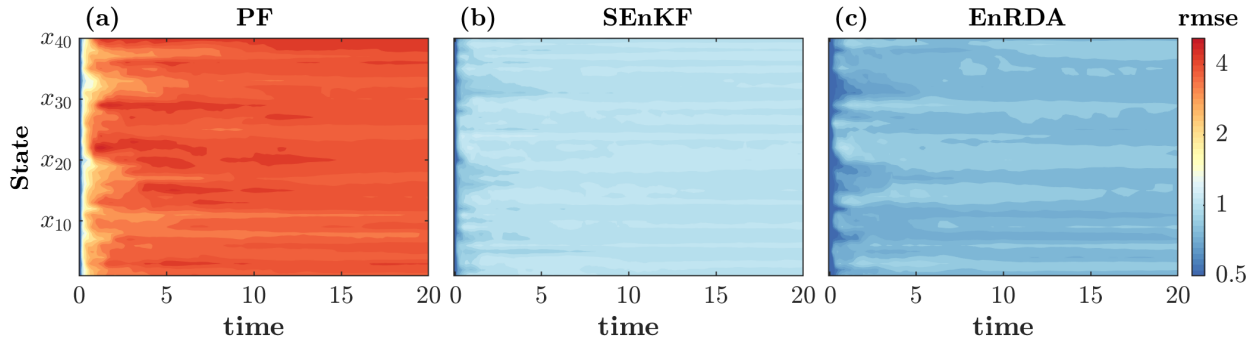


Figure 3: Temporal evolution of the root mean-squared error (rmse) for the (a) Particle Filter (PF) with 5000 particles, (b) Stochastic Ensemble Kalman Filter (SEnKF), and (c) Ensemble Riemannian Data Assimilation (EnRDA) each with 50 ensemble members in 40-dimensional Lorenz-96 system. The results report the mean values of 50 independent simulations.

308 As previously noted, the displacement parameter  $\eta$  plays an important role in EnRDA as  
 309 it controls the shape and position of the analysis state distribution relative to the background  
 310 distribution and the normalized likelihood function. Currently, there exists no known closed-  
 311 form solution for optimal approximation of this parameter. Therefore, in this paper, we focus  
 312 on determining its optimal value through heuristic cross-validation by an offline bias-variance  
 313 trade-off analysis. Specifically, we quantify the rmse of the EnRDA analysis state for different  
 314 values of  $\eta$  for 50 independent simulations.

315 The bias and rmse, together with their respective 5<sup>th</sup>–95<sup>th</sup> percentile bounds, as functions  
 316 of the displacement parameter  $\eta$  are shown in Figure 4a. As explained earlier, when  $\eta$   
 317 increases, the analysis distribution moves towards the background distribution. Since the  
 318 background state is systematically biased due to the erroneous external forcing, the analysis  
 319 bias increases monotonically with  $\eta$ ; while the rmse shows a minimum point. Therefore, there  
 320 exists a form of bias-variance trade-off in the analysis error, which leads to an approximation

321 of an optimal value of  $\eta$  based on a minimum rmse criterion. It is important to note that the  
 322 background uncertainty and thus the optimal value of  $\eta$  varies in response to the ensemble  
 323 size as shown in Figure 4b. The reason is that a larger number of ensemble members reduces  
 324 the uncertainty in the characterization of the background, but the bias is not affected. To  
 325 compensate, a larger optimal value for  $\eta$  is needed. This optimal value approaches an  
 326 asymptotic value as the ensemble sample size increases and will achieve the highest value at  
 327 the limit  $M \rightarrow \infty$ , when the sample moments converge to the biased forecast moments.

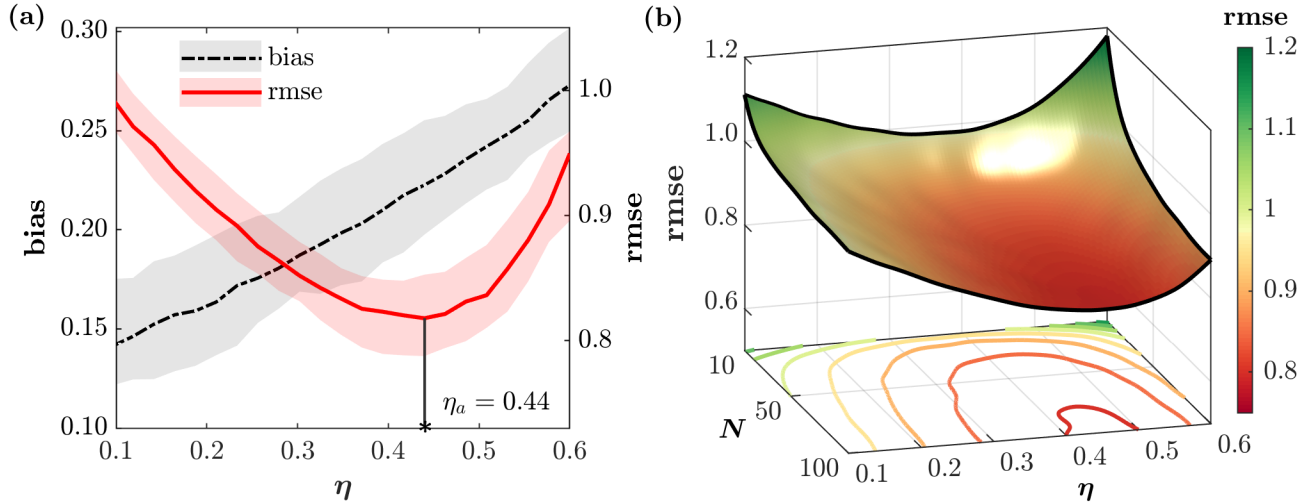


Figure 4: (a) Bias and root mean-squared error (rmse) for a range of displacement parameter  $\eta \in [0.1, 0.6]$  in Ensemble Riemannian Data Assimilation (EnRDA) with 50 ensemble members, obtained across 40-dimensions of the Lorenz-96 system. The shaded regions indicate the 5<sup>th</sup>–95<sup>th</sup> percentile bound for the respective error metrics obtained from 50 independent simulations. (b) Variation of rmse as a function of the number of ensemble members and  $\eta$ .

328 One may argue that such a tuning favors EnRDA since it explicitly accounts for the effects  
 329 of bias, either in background or observations, while there is no bias correction mechanism in  
 330 the implementation of the SEnKF and the PF. To make a fairer comparison, we investigate an  
 331 alternative approach to approximate the displacement parameter solely based on the known  
 332 error covariance matrices at each assimilation cycle. Recalling that in classic DA, the analysis  
 333 state is essentially the Euclidean barycenter, where the relative weights of the background  
 334 state and observations are optimally characterized based on the error covariances under  
 335 zero bias assumptions. However, over the Wasserstein space, the displacement parameter  
 336 determines the weight between the entire distribution of the background and the normalized  
 337 likelihood function. Theoretically, knowing the Wasserstein distances from ground truth to  
 338 both likelihood function and forecast distribution enables to obtain an optimal value for  
 339  $\eta$ . Even though such distances are not known in reality, the total Wasserstein distance  
 340 between the normalized likelihood function and the forecast distribution is known at each  
 341 assimilation cycle. Therefore, given an estimate of the distance between the ground truth  
 342 and the normalized likelihood function or the forecast distribution, leads to an approximation  
 343 of  $\eta$ .

344 It is known that the square of the Wasserstein distance between two equal-mean Gaus-

345 sian distributions  $\mathcal{N}(\boldsymbol{\mu}, \boldsymbol{\Sigma}_1)$  and  $\mathcal{N}(\boldsymbol{\mu}, \boldsymbol{\Sigma}_2)$  is  $d_{\mathcal{W}}^2 = \text{tr}(\boldsymbol{\Sigma}_1 + \boldsymbol{\Sigma}_2 - 2(\boldsymbol{\Sigma}_1^{\frac{1}{2}}\boldsymbol{\Sigma}_2\boldsymbol{\Sigma}_1^{\frac{1}{2}})^{\frac{1}{2}})$  (Y. Chen  
 346 et al., 2019). Therefore, under the assumption that only the background state is biased,  
 347 the square of the Wasserstein distance between the true state  $\mathbf{x}_{tr}$ , as a Dirac delta func-  
 348 tion, and the normalized likelihood function reduces to  $\text{tr}(\mathbf{R})$ . At the same time, the  
 349 square of the Wasserstein distance between the normalized likelihood function and fore-  
 350 cast distribution is  $\text{tr}(\mathbf{C}^T\mathbf{U}^a)$ . Therefore, we can approximate the interpolation parameter  
 351 as  $\bar{\eta}_a = \text{tr}(\mathbf{R}) (\text{tr}(\mathbf{C}^T\mathbf{U}^a) + \text{tr}(\mathbf{R}))^{-1}$  without any explicit *a priori* knowledge of bias.

352 Comparisons of the rmse values for the studied DA methodologies as a function of ensem-  
 353 ble size are shown in Figure 5. For EnRDA, the displacement parameter is obtained from the  
 354 bias-aware cross-validation ( $\eta = 0.44$ , EnRDA-I) and from the known error covariances as  
 355 explained above (EnRDA-II). The SEnKF and EnRDA result in smaller error metrics with  
 356 a much smaller ensemble size than PF. As seen, EnRDA can perform well even for smaller  
 357 ensemble sizes as low as 20. Its results quickly stabilize with more than 40 ensemble members  
 358 and exhibit a marginal improvement over the SEnKF (12–24%) in the presence of bias. The  
 359 rmse of the SEnKF also stabilizes quickly but remains above the standard deviation of the  
 360 observation error indicating that in the presence of bias, the lowest possible variance, known  
 361 as the Cramer-Rao Lower Bound (Cramér, 1999; Rao et al., 1973) cannot be met.

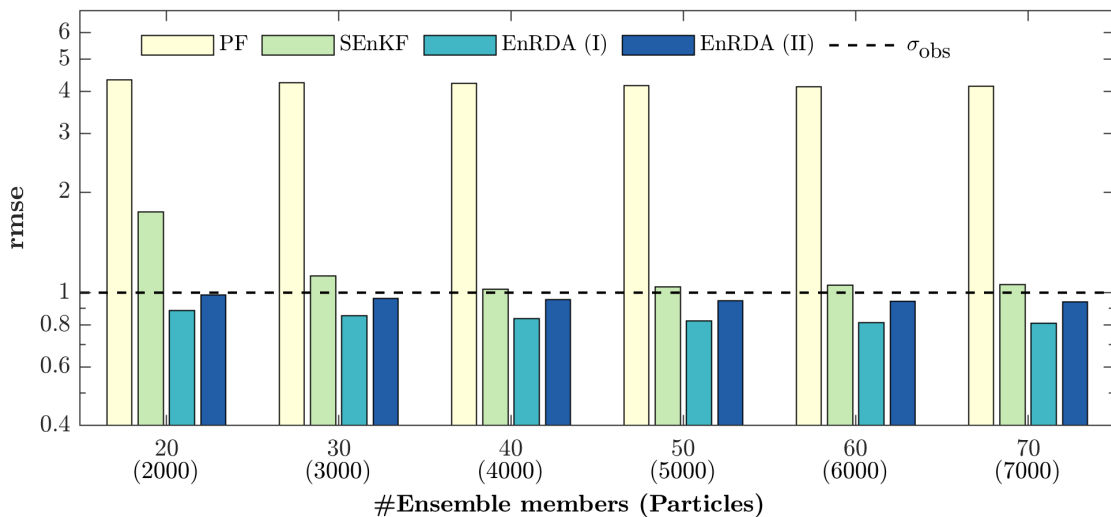


Figure 5: The root mean-squared error (rmse) for the different number of ensemble members/particles in the Particle Filter (PF), Stochastic Ensemble Kalman Filter (SEnKF), and Ensemble Riemannian Data Assimilation (EnRDA) when the displacement parameter is obtained from bias-aware cross-validation (ENRDA-I) and a dynamic approach without *a priori* knowledge of bias (EnRDA-II) for Lorenz-96 system. The dashed line is the standard deviation of the observation error.

362 It is also important to note that the higher rmse of the PF compared to the SEnKF and  
 363 EnRDA is due to the problem of filter degeneracy which is further exacerbated by the pres-  
 364 ence of systematic errors in model forecasts (Poterjoy & Anderson, 2016). To alleviate this  
 365 problem, one may investigate the use of methodologies suggested in recent years including  
 366 the auxiliary particle filter where the weights of the particles at each assimilation cycle are

367 defined based on the likelihood function from the next cycle using a pre-model run (Pitt &  
 368 Shephard, 1999), the backtracking particle filter in which the analysis state is backtracked  
 369 to identify the time step when the filter became degenerate (Spiller et al., 2008) as well as  
 370 sampling from a transition density to pull back particles towards observations (van Leeuwen,  
 371 2010).

## 372 4.2 Quasi-Geostrophic Model

373 The multilayered quasi-geostrophic (QG, Pedlosky et al., 1987) model is known as one of the  
 374 simplest circulation models capable of providing a reasonable representation of the mesoscale  
 375 variability in geophysical flows. In its simplified form, the QG model describes the conser-  
 376 vation of potential vorticity  $\{\zeta_k\}_{k=1}^K$  in  $K$  vertically-mixed vertical layers:

$$\left( \frac{\partial}{\partial t} + u_k \frac{\partial}{\partial \lambda} + v_k \frac{\partial}{\partial \phi} \right) \zeta_k = 0, \quad k = 1, \dots, K, \quad (9)$$

377 where  $u_k = -\frac{\partial \Psi_k}{\partial \phi}$  and  $v_k = \frac{\partial \Psi_k}{\partial \lambda}$  represent the zonal and meridional components of the  
 378 velocity field, obtained from the geostrophic approximation;  $\{\Psi_k\}_{k=1}^K$  is the streamfunction  
 379 in  $K$  layers; and  $\lambda$  and  $\phi$  are the zonal and meridional coordinates, respectively.

380 For a two-layer QG model ( $K = 2$ ), the potential vorticity at any time step is the sum  
 381 of the relative vorticity, the planetary vorticity and the stretching term, given by:

$$\zeta_k = \nabla^2 \Psi_k + f + (1 - 2\delta_{2k}) \frac{f_0^2}{g' h_k} (\Psi_2 - \Psi_1) \quad k = 1, \dots, 2, \quad (10)$$

382 where  $\nabla^2(\cdot) = \frac{\partial^2(\cdot)}{\partial \lambda^2} + \frac{\partial^2(\cdot)}{\partial \phi^2}$  is the Laplace operator,  $f = f_0 + \beta(\phi - \phi_0)$  is the Coriolis  
 383 parameter linearly varying with the meridional coordinate  $\phi$  ( $\beta$ -plane approximation),  $f_0$  is  
 384 the Coriolis parameter at mid-basin where  $\phi = \phi_0$ ,  $g' = \frac{g(\rho_2 - \rho_1)}{\rho_2}$  is the reduced value of  
 385 the gravitational acceleration  $g$ ,  $\rho_k$  and  $h_k$  are the density and thickness of the  $k^{\text{th}}$  layer,  
 386 respectively. The QG model has been the subject of numerous experiments to test the  
 387 performance of DA techniques (Cotter et al., 2020; Evensen, 1994b; Evensen & Van Leeuwen,  
 388 1996; Fisher & Gürol, 2017; Penny et al., 2019).

### 389 4.2.1 Experimental Setup, Results and Discussion

390 Due to the high-dimensionality of the QG model and the well-known problem of filter de-  
 391 generacy in the PF, we chose to omit its application on the QG model. Similar to the study  
 392 conducted in (Evensen, 1992, 1994b), the streamfunction is chosen as the state variable for  
 393 the DA experiments. The streamfunction field, at each vertical layer, is discretized over a  
 394 uniform grid of dimension  $m_\lambda \times m_\phi$  with spacing of  $\Delta\lambda = \Delta\phi = 100$  km, where  $m_\lambda = 65$  and  
 395  $m_\phi = 33$ . The model domain is assumed to have periodic boundaries along the zonal direction  
 396 and free-slip conditions, that is,  $v_k = 0, \forall k$ , holds on the northern and southern boundaries.  
 397 The standard model parameter values of  $f_0 = 7.28 \times 10^{-5} \text{ s}^{-1}$ ,  $\beta = 2 \times 10^{-11} \text{ m}^{-1} \text{ s}^{-1}$ , and

398  $g = 9.81 \text{ m s}^{-2}$  are used. The total depth of the atmospheric column is set to 10 km with  
 399 depths and densities of top and bottom layer as  $h_1 = h_2 = 5 \text{ km}$ , and  $\rho_1 = 1$  and  $\rho_2 = 1.05$   
 400  $\text{kg m}^{-3}$ , respectively. We first initialize the streamfunction in the two layers as a function of  
 401 the zonal and meridional coordinates by setting  $\Psi_1(\lambda, \phi) = -12.5 \times 10^6 \tan^{-1} (20(\phi/\Delta\phi -$   
 402  $m_\phi/2)m_\phi^{-1}) - 1.25 \times 10^6 \sin (2\pi(\lambda/\Delta\lambda - 1)m_\lambda^{-1}) \sin^2 (2\pi(\phi/\Delta\phi - 1)(m_\phi - 1)^{-1}) \text{ m}^2 \text{ s}^{-1}$  and  
 403  $\Psi_2(\lambda, \phi) = 0.3 \Psi_1(\lambda, \phi)$ .

404 From the initial value of the streamfunction field in each layer, potential vorticity is  
 405 obtained using a nine-point second-order finite difference scheme to compute the Laplacian  
 406 in Equation 10. The model in Equation 9 is then integrated with a time step of  $\Delta t = 0.5 \text{ hr}$   
 407 using the fourth-order Runge-Kutta approximation to advect and obtain potential vorticity  
 408 at internal grid points for the next time step. The streamfunction at the next time step is  
 409 then calculated from this potential vorticity by solving the set of the Helmholtz equations  
 410 (Equation 10). To avoid any form of initial transient behavior and to create vortex structures  
 411 in the streamfunction, the QG model is integrated first for 720 time steps and then the  
 412 endpoint of the run is used as the initial condition for subsequent DA experimentation.

413 The ground truth of the streamfunction is obtained by integrating the QG model with  
 414 a time step of  $\Delta t$  over a time period of  $T = 0 - 15 \text{ day}$  in the absence of any model error.  
 415 Observations are assumed to be available at an assimilation time interval of  $24\Delta t$  or 12 hr.  
 416 To construct observations, representative, random and systematic errors are applied to the  
 417 ground truth. The representative error is applied by lowering the resolution of the ground  
 418 truth through box averaging over a window of size  $n_\lambda \times n_\phi$ , where  $n_\lambda = 5$  and  $n_\phi = 3$ . Then  
 419 a heteroscedastic biased Gaussian noise with mean (standard deviation)  $0.6 \times 10^6 \text{ m}^2 \text{ s}^{-1}$ ,  
 420 equivalent to 33 (10%) of the mean magnitude of the ground truth is applied.

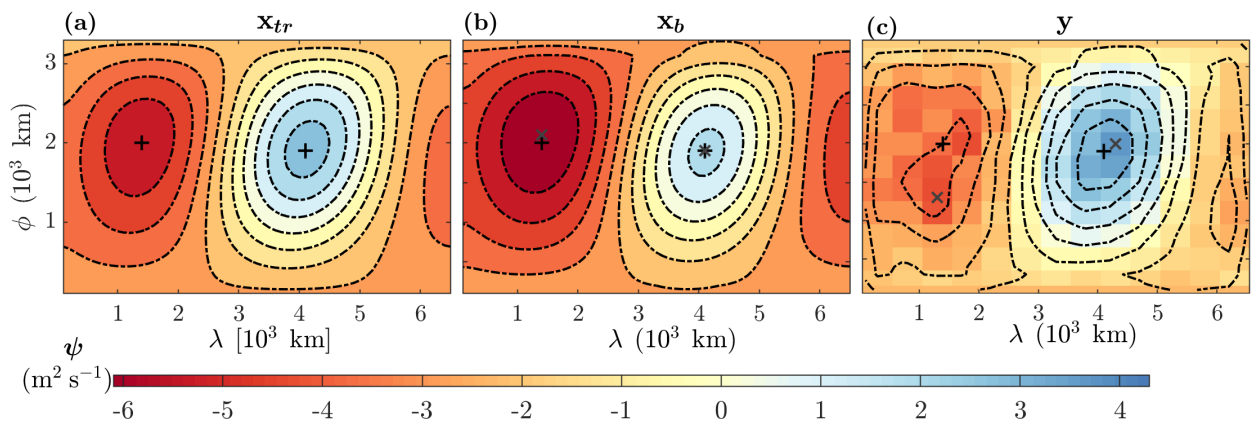


Figure 6: (a) The true state  $\mathbf{x}_{tr}$ , (b) background state  $\mathbf{x}_b$ , and (c) observations  $\mathbf{y}$  for bottom layer field of streamfunction in the quasi-geostrophic model at first assimilation cycle  $T = 12 \text{ hr}$ . The black plus (grey cross) signs show the location of the global extrema for the true state (background and observation).

421 To characterize the distribution of the background state, 50 ensemble members for both  
 422 SEnKF and EnRDA are generated using model errors  $\boldsymbol{\omega}_t \sim \mathcal{N}(0, \alpha \sigma_t^2 \mathbf{I}_{m_\lambda \times m_\phi})$  for each layer  
 423 with  $\sigma_0^2 = 10^8 \text{ m}^4 \text{ s}^{-2}$  and  $\sigma_t^2 = 5 \times 10^6 \text{ m}^4 \text{ s}^{-2}$  for  $t > 0$ , where the factor  $\alpha \in [0, 1]$  grows  
 424 linearly from 0 at the northern and southern boundaries to 1 at mid-basin. To introduce

425 systematic errors in the forecast, we utilize a multiplicative error of 0.015% in the QG model  
 426 by multiplying the potential vorticity obtained from Equation 10 at every  $\Delta t$  with a factor  
 427 of 1.00015. At each assimilation cycle,  $N = 500$  samples of the observations are obtained by  
 428 perturbing the observations with the heteroscedastic Gaussian noise with standard deviation  
 429 10% of the mean magnitude of the ground truth.

430 In the SEnKF, to alleviate the well-known problem of undersampling (J. L. Anderson,  
 431 2012) and improve its performance, we utilize covariance inflation (J. L. Anderson & An-  
 432 derson, 1999) and localization (Hamill, 2001; Houtekamer & Mitchell, 2001) as discussed in  
 433 Appendix A.2. For EnRDA, similar to the Lorenz-96 setup (Section 4.1.1), the displacement  
 434 parameter is set to  $\eta = 0.4$  through a cross-validation study based on a minimum rmse  
 435 criterion as shown in Table 1. To increase the robustness of the inference about the results,  
 436 the quality metrics are averaged using 10 simulations with different random realizations.

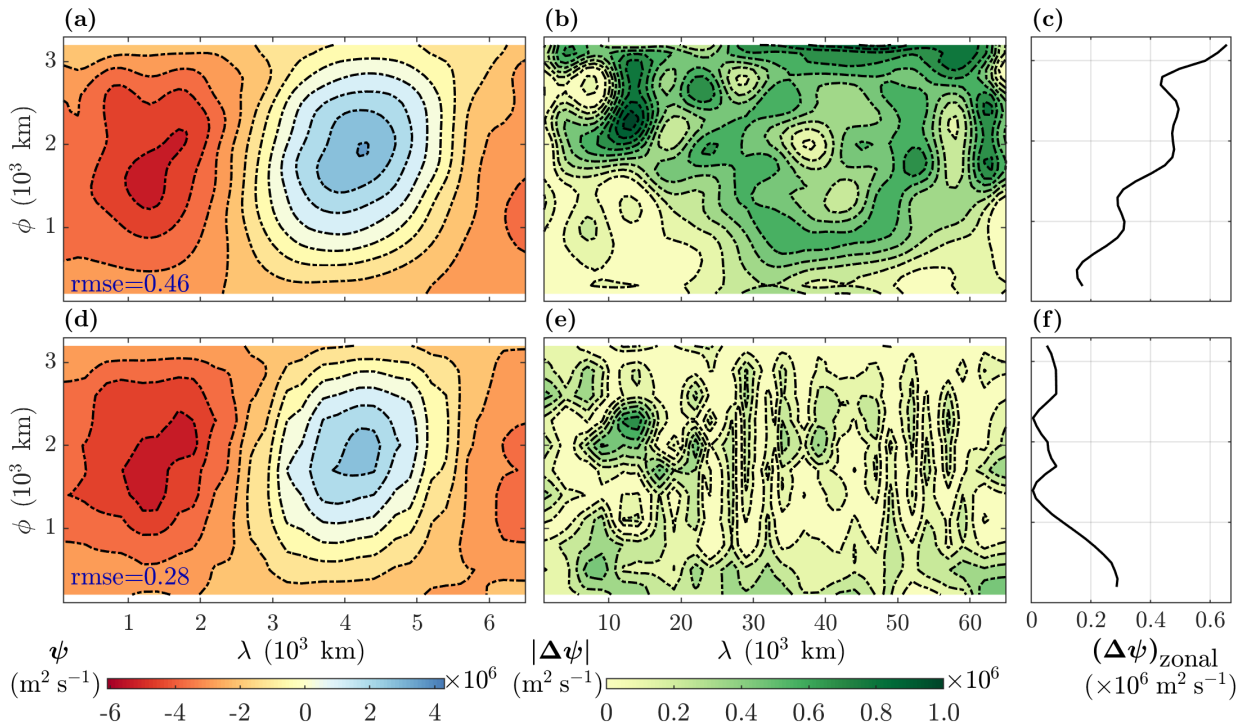


Figure 7: The streamfunction analysis state  $\mathbf{x}_a$  by (a) Stochastic Ensemble Kalman Filter (SEnKF), and (d) Ensemble Riemannian Data Assimilation (EnRDA) as well as (b, e) their respective absolute error fields and (c, f) zonal mean of the error for the bottom layer of quasi-geostrophic model, at the first assimilation cycle  $T = 12$  hr. The root mean-squared error (rmse) values ( $\times 10^6 m^2 s^{-1}$ ) for the entire fields are also reported in (a) and (d).

437 The true state, background state, and the observations of the bottom layer streamfunction  
 438 at the first assimilation cycle  $T = 12$  hr are shown in Figure 6. It can be seen that both the  
 439 background state and the observations show possible systematic biases as the position and  
 440 the values of their global extrema are significantly different from the ground truth.

441 The results of the DA experiments using the SEnKF and EnRDA at the first assimilation  
 442 cycle for the bottom layer are also shown in Figure 7. It can be seen that, in the SEnKF,  
 443 the streamfunction values are slightly overestimated, signaling the persistence of bias in the

Table 1: Average root mean-squared error (rmse) values as a function of the displacement parameter  $\eta \in [0.25, 0.6]$  for Ensemble Riemannian Data Assimilation (EnRDA) from 10 independent simulations of the two-layer quasi-geostrophic model.

	rmse ( $\times 10^6 \text{ m}^2 \text{ s}^{-1}$ )							
$\eta$	0.25	0.30	0.35	0.40	0.45	0.50	0.55	0.60
Top layer	0.283	0.260	0.255	0.242	0.250	0.258	0.309	0.369
Bottom layer	0.211	0.198	0.194	0.189	0.206	0.222	0.294	0.368
Average	0.247	0.229	0.224	0.215	0.228	0.240	0.301	0.369

444 analysis state (Figure 7a). This is further evident as the analysis error field is coherent and  
 445 structured (Figure 7b). On the other hand, it appears that EnRDA (Figure 7d) results in  
 446 a more incoherent error field with a reduced bias (Figure 7e). The rmse for the EnRDA  
 447 ( $0.28 \times 10^6 \text{ m}^2 \text{ s}^{-1}$ ) is lower than the one by the SEnKF ( $0.46 \times 10^6 \text{ m}^2 \text{ s}^{-1}$ ). However, the  
 448 difference between the two methods shrinks over  $T = 0 - 15$  days and the mean analysis rmse  
 449 over both layers by the EnRDA (SEnKF) reaches  $0.21 \times 10^6$  ( $0.25 \times 10^6$ )  $\text{m}^2 \text{ s}^{-1}$ . Furthermore,  
 450 in the SEnKF, due to the presence of systematic error, the zonal mean of the absolute error  
 451 is consistently higher than that of the EnRDA, see (Figure 7c and f).

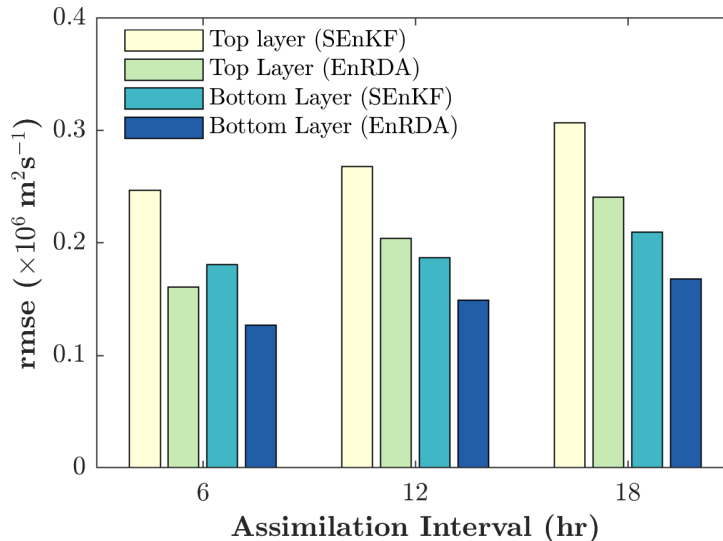


Figure 8: The average root mean-squared error (rmse) values as a function of assimilation intervals 6, 12 and 18 hr in the Stochastic Ensemble Kalman Filter (SEnKF) and Ensemble Riemannian Data Assimilation (EnRDA) for the two-layer quasi-geostrophic model.

452 We further examined the performance of the EnRDA and the SEnKF on the QG model  
 453 with a  $\pm 50\%$  change in the assimilation interval of 12 hr as shown in Figure 8. To make  
 454 the comparison fair between different assimilation intervals which have a different number  
 455 of assimilation cycles and to eliminate the impact of transient behavior, we only report the  
 456 statistics for the last 15 assimilation steps. With the increase in assimilation interval, the

457 systematic error grows in the forecast largely due to the multiplicative error being added  
458 to the forecast at every time step. Therefore, as is expected, with the increase in assimila-  
459 tion interval, the rmse grows monotonically and the performance of the DA methodologies  
460 degrades. However, the EnRDA demonstrates consistent improvement over a bias-blind  
461 implementation of the SEnKF (20–33%) across the range of assimilation intervals.

## 462 5 Summary and Concluding Remarks

463 In this study, we discussed recasting geophysical data assimilation (DA) as a barycenter  
464 problem over the Wasserstein space with Riemannian geometry, in an ensemble setting. The  
465 DA methodology, called the Ensemble Riemannian Data Assimilation (EnRDA), enables to  
466 obtain the analysis state probability distribution through optimal transportation of proba-  
467 bility masses between the background distribution and the normalized likelihood function.  
468 We demonstrated that this approach does not rely on any parametric assumptions about  
469 the distributions. Unlike DA over the Euclidean space, this approach does not guarantee a  
470 minimum mean squared approximation of the analysis when the model and observations are  
471 unbiased. However, it can formally correct systematic errors by allowing for a smooth tran-  
472 sition between the background distribution and the normalized likelihood function over the  
473 Wasserstein space. Therefore, we hypothesized that under a biased state space, EnRDA can  
474 lead to reduced uncertainty of the analysis state compared to classic DA over the Euclidean  
475 space with no ad-hoc bias correction.

476 We verified the hypothesis by applying the EnRDA to the 40-dimensional chaotic Lorenz-  
477 96 system and a two-layer quasi-geostrophic representation of atmospheric circulation. Al-  
478 though initial comparisons of EnRDA with classic DA methodologies, in our case, the  
479 Stochastic Ensemble Kalman Filter and the Particle Filter, suggested improved performance,  
480 further comprehensive comparisons with bias-aware versions of the Euclidean DA method-  
481 ologies are required to fully characterize the pros and cons of DA over the Wasserstein space.  
482 We need to emphasize that in the absence of systematic errors, Euclidean DA methodologies  
483 is likely to achieve improved performance over EnRDA in terms of the mean squared error.  
484 However, one of the advantages of the EnRDA is that it is a fully nonlinear DA method,  
485 and it does not require any localization procedure.

486 One of the major weaknesses of the presented methodology in its current form is that  
487 all dimensions of the problem are assumed to be observable. This is an important issue  
488 when it comes to the assimilation of sparse data. Future research is needed to address  
489 partial observability in DA over the Wasserstein space. A possible direction is through  
490 multi-marginal optimal mass transport (Pass, 2015), which could enable to couple different  
491 dimensions of the problem and propagate the information content of sparse observations  
492 to unobserved dimensions. Moreover, currently, the displacement parameter is constant  
493 across multiple dimensions of the problem. Future research is needed to understand how the  
494 displacement parameter can be estimated differently depending on the error structure across  
495 different dimensions of the state space. Another option is to perform the EnRDA only in that  
496 part of the state space that is directly observed and use the ensemble covariance to update  
497 the unobserved part of state space, similar to a SEnKF. We anticipate that expanding the  
498 application of the presented methodology for assimilating satellite data into land-atmosphere

499 models could be another useful future direction of research given the fact that these models  
500 are often markedly biased (Chepurin et al., 2005; Dee & Da Silva, 1998; De Lannoy et al.,  
501 2007; Lin et al., 2017).

## 502 A Appendix

### 503 A.1 Sinkhorn’s Algorithm for Optimal Mass Transport

504 To solve the regularized optimal mass transport problem in Equation 7, we utilize Sinkhorn’s  
505 algorithm (Sinkhorn, 1967). To that end, first, the Lagrangian form of the Equation 7 using  
506 two Lagrange multipliers  $\mathbf{a} \in \mathbb{R}^M$  and  $\mathbf{b} \in \mathbb{R}^N$  is obtained as follows:

$$\mathcal{L}(\mathbf{U}, \mathbf{a}, \mathbf{b}) = \text{tr}(\mathbf{C}^T \mathbf{U}) - \gamma \text{tr}(\mathbf{U}^T [\log(\mathbf{U} - \mathbb{1}_M \mathbb{1}_N^T)]) - \mathbf{a}^T (\mathbf{U} \mathbb{1}_N - \mathbf{p}_x) - \mathbf{b}^T (\mathbf{U}^T \mathbb{1}_M - \tilde{\mathbf{p}}_{y|x}). \quad (11)$$

507 Now, we set the first-order derivative of the Lagrangian form in Equation 11, with respect  
508 to  $(i, j)^{\text{th}}$  element of the joint distribution  $(u_{ij})$  to zero:

$$\frac{\partial \mathcal{L}(\mathbf{U}, \mathbf{a}, \mathbf{b})}{\partial u_{ij}} = c_{ij} + \gamma \log(u_{ij}) - a_i - b_j = 0 \quad \forall i, j, \quad (12)$$

509 which ultimately leads to  $u_{ij} = \exp\left(\frac{a_i}{\gamma}\right) \exp\left(-\frac{c_{ij}}{\gamma}\right) \exp\left(\frac{b_j}{\gamma}\right)$ . This can be rewritten  
510 in a matrix form as  $\mathbf{U}^a = \text{diag}(\mathbf{s}) \mathbf{V} \text{diag}(\mathbf{t})$ , where  $\left\{ \mathbf{V} \in \mathbb{R}_+^{M \times N} : v_{ij} = \exp\left(-\frac{c_{ij}}{\gamma}\right) \right\}$   
511 is the Gibb’s kernel of the cost matrix  $\mathbf{C}$ , and  $\mathbf{s} \in \mathbb{R}^M$ ,  $\mathbf{t} \in \mathbb{R}^N$  are the unknown scaling  
512 vectors. The notation  $\text{diag}(\mathbf{x}) \in \mathbb{R}^{M \times M}$  represents a diagonal matrix with its diagonal entries  
513 provided by  $\mathbf{x} \in \mathbb{R}^M$ .

514 By setting the derivatives of the Lagrangian with respect to the Lagrange multipliers as  
515 zero we recover the two conditions, which we can write as  $\mathbf{p}_x = \text{diag}(\mathbf{s}) \mathbf{V} \text{diag}(\mathbf{t}) \mathbb{1}_N$  and  
516  $\tilde{\mathbf{p}}_{y|x} = \text{diag}(\mathbf{t}) \mathbf{V}^T \text{diag}(\mathbf{s}) \mathbb{1}_M$  leading to:

$$\mathbf{s} = \mathbf{p}_x \oslash (\mathbf{V} \mathbf{t}) \quad \text{and} \quad \mathbf{t} = \tilde{\mathbf{p}}_{y|x} \oslash (\mathbf{V}^T \mathbf{s}), \quad (13)$$

517 where the notation  $\mathbf{x} \oslash \mathbf{y}$  represents a Hadamard element-wise division of equal length vectors.  
518 The form presented in Equation 13 is known as the matrix scaling problem (Borobia & Cantó,  
519 1998) and can be efficiently solved iteratively:

$$\mathbf{s}^{(i)} = \mathbf{p}_x \oslash (\mathbf{V} \mathbf{t}^{(i-1)}) \quad \text{and} \quad \mathbf{t}^{(i)} = \tilde{\mathbf{p}}_{y|x} \oslash (\mathbf{V}^T \mathbf{s}^{(i)}), \quad (14)$$

520 where  $i$  is the iteration count and the algorithm is initialized with a positive vector  $\mathbf{t}^{(0)} = \mathbb{1}_N$ .  
521 In our implementation, we set the iteration termination criterion as  $\frac{\|\mathbf{s}^{(i)} - \mathbf{s}^{(i-1)}\|_2}{\|\mathbf{s}^{(i-1)}\|_2} \leq 10^{-4}$   
522 or  $i > 300$ . After the convergence of the solution for  $\mathbf{s}$  and  $\mathbf{t}$ , the optimal joint distribution  
523 can be obtained as  $\mathbf{U}^a = \text{diag}(\mathbf{s}) \mathbf{V} \text{diag}(\mathbf{t})$ .

## A.2 Covariance Inflation and Localization in Ensemble Kalman Filter

The ensemble size in the Stochastic Ensemble Kalman filter (SEnKF), if much smaller than the state dimension, such as in the presented case of the quasi-geostrophic model, leads to underestimation of the forecast error covariance matrix and subsequently filter divergence problems. To alleviate this problem, a covariance inflation procedure can be implemented by multiplying the forecast error covariance matrix by an inflation factor  $\tau > 1$  (J. L. Anderson & Anderson, 1999) where its optimal value depend on the ensemble size (Hamill et al., 2001) and other characteristics of the problem at hand.

The covariance localization procedure in the SEnKF further attempts to improve its performance by ignoring the spurious long-range dependence in the ensemble background covariance by applying a prespecified cutoff threshold on the correlation structure of the field. An SEnKF equipped with a tuned localization procedure can be efficiently used in high-dimensional atmospheric and ocean models even with less than 100 ensemble members (J. L. Anderson, 2012). The covariance localization in an SEnKF is accomplished by modifying the Kalman gain matrix  $\mathbf{K} \in \mathbb{R}^{m \times m}$  through implementation of a Hadamard element-wise product of the forecast error covariance matrix  $\mathbf{B} \in \mathbb{R}^{m \times m}$  with a distance-based correlation matrix  $\boldsymbol{\rho} \in \mathbb{R}^{m \times m}$ :

$$\mathbf{K} = (\boldsymbol{\rho} \odot \mathbf{B})\mathbf{H}^T(\mathbf{H}(\boldsymbol{\rho} \odot \mathbf{B})\mathbf{H}^T + \mathbf{R})^{-1}, \quad (15)$$

where  $\mathbf{X} \odot \mathbf{Y}$  represent the Hadamard element-wise product between equal size matrices  $\mathbf{X}$  and  $\mathbf{Y}$ .

Following the work of Gaspari & Cohn (1999), we utilized the fifth-order piece-wise rational function that depends on a single length scale parameter  $d$  and an Euclidean distance matrix  $\{\mathbf{L} \in \mathbb{R}^{m \times m} : l_{ij} = \|x_i - x_j\|_2\}$  for obtaining the  $(i, j)^{\text{th}}$ -element of the localizing correlation matrix  $\boldsymbol{\rho}$ :

$$\rho_{ij} = \begin{cases} -\frac{1}{4}r^5 + \frac{1}{2}r^4 + \frac{5}{8}r^3 - \frac{5}{3}r^2 + 1, & 0 \leq r \leq 1, \\ \frac{1}{12}r^5 - \frac{1}{2}r^4 + \frac{5}{8}r^3 + \frac{5}{3}r^2 - 5r + 4 - \frac{2}{3}r^{-1}, & 1 < r \leq 2, \\ 0, & r > 2, \end{cases} \quad (16)$$

where  $r = \frac{l_{ij}}{d}$ , and  $d$  is the length scale.

In our implementation of the SEnKF in the QG model, the inflation factor and length scale were chosen between  $\tau = 1.01 - 1.08$  and  $d = 400 - 1800$  [km] respectively depending on the experimental setup through trial and error analysis to minimize the root mean-squared error.

## 553 Acknowledgements

554 Data archiving is underway at the Data Repository for University of Minnesota ([https://](https://conservancy.umn.edu/handle/11299/166578)  
555 [conservancy.umn.edu/handle/11299/166578](https://conservancy.umn.edu/handle/11299/166578)). The first and second author acknowledge  
556 the grant from the National Aeronautics and Space Administration (NASA) Terrestrial Hy-  
557 drology Program (THP, 80NSSC18K1528) and the New (Early Career) Investigator Pro-  
558 gram (NIP, 80NSSC18K0742). The third author acknowledges support from the Euro-  
559 pean Research Council for funding via the Horizon2020 CUNDA project under number  
560 694509. The fourth author also acknowledges support from National Science Foundation  
561 (NSF, DMS1830418).

## 562 References

- 563 Agueh, M., & Carlier, G. (2011). Barycenters in the wasserstein space. *SIAM Journal on*  
564 *Mathematical Analysis*, 43(2), 904–924.
- 565 Altman, A., & Gondzio, J. (1999). Regularized symmetric indefinite systems in interior  
566 point methods for linear and quadratic optimization. *Optimization Methods and Software*,  
567 11(1-4), 275–302.
- 568 Anderson, J., & Lei, L. (2013). Empirical localization of observation impact in ensemble  
569 kalman filters. *Monthly Weather Review*, 141(11), 4140–4153.
- 570 Anderson, J. L. (2001). An ensemble adjustment kalman filter for data assimilation. *Monthly*  
571 *weather review*, 129(12), 2884–2903.
- 572 Anderson, J. L. (2012). Localization and sampling error correction in ensemble kalman filter  
573 data assimilation. *Monthly Weather Review*, 140(7), 2359–2371.
- 574 Anderson, J. L. (2016). Reducing correlation sampling error in ensemble kalman filter data  
575 assimilation. *Monthly Weather Review*, 144(3), 913–925.
- 576 Anderson, J. L., & Anderson, S. L. (1999). A monte carlo implementation of the nonlin-  
577 ear filtering problem to produce ensemble assimilations and forecasts. *Monthly Weather*  
578 *Review*, 127(12), 2741–2758.
- 579 Bigot, J., Klein, T., et al. (2012). Consistent estimation of a population barycenter in the  
580 wasserstein space. *ArXiv e-prints*, 49.
- 581 Bishop, C. H., Etherton, B. J., & Majumdar, S. J. (2001). Adaptive sampling with the  
582 ensemble transform kalman filter. part i: Theoretical aspects. *Monthly weather review*,  
583 129(3), 420–436.
- 584 Borobia, A., & Cantó, R. (1998). Matrix scaling: A geometric proof of sinkhorn’s theorem.  
585 *Linear algebra and its applications*, 268, 1–8.
- 586 Brajard, J., Carrassi, A., Bocquet, M., & Bertino, L. (2020). Combining data assimilation  
587 and machine learning to emulate a dynamical model from sparse and noisy observations:  
588 a case study with the lorenz 96 model. *Journal of Computational Science*, 44, 101171.

- 589 Brenier, Y. (1987). Décomposition polaire et réarrangement monotone des champs de  
590 vecteurs. *CR Acad. Sci. Paris Sér. I Math.*, 305, 805–808.
- 591 Burgers, G., Jan van Leeuwen, P., & Evensen, G. (1998). Analysis scheme in the ensemble  
592 kalman filter. *Monthly weather review*, 126(6), 1719–1724.
- 593 Chen, B., Dang, L., Gu, Y., Zheng, N., & Principe, J. C. (2019). Minimum error entropy  
594 kalman filter. *arXiv preprint arXiv:1904.06617*.
- 595 Chen, J., Chen, Y., Wu, H., & Yang, D. (2018). The quadratic wasserstein metric for  
596 earthquake location. *Journal of Computational Physics*, 373, 188–209.
- 597 Chen, Y., Georgiou, T. T., & Tannenbaum, A. (2017). Matrix optimal mass transport: a  
598 quantum mechanical approach. *IEEE Transactions on Automatic Control*, 63(8), 2612–  
599 2619.
- 600 Chen, Y., Georgiou, T. T., & Tannenbaum, A. (2018a). Optimal transport for gaussian  
601 mixture models. *IEEE Access*, 7, 6269–6278.
- 602 Chen, Y., Georgiou, T. T., & Tannenbaum, A. (2018b). Wasserstein geometry of quantum  
603 states and optimal transport of matrix-valued measures. In *Emerging applications of*  
604 *control and systems theory* (pp. 139–150). Springer.
- 605 Chen, Y., Georgiou, T. T., & Tannenbaum, A. (2019). Optimal transport for gaussian  
606 mixture models. *IEEE Access*, 7, 6269–6278.
- 607 Chepurin, G. A., Carton, J. A., & Dee, D. (2005). Forecast model bias correction in ocean  
608 data assimilation. *Monthly weather review*, 133(5), 1328–1342.
- 609 Chianese, E., Galletti, A., Giunta, G., Landi, T., Marcellino, L., Montella, R., & Riccio,  
610 A. (2018). Spatiotemporally resolved ambient particulate matter concentration by fus-  
611 ing observational data and ensemble chemical transport model simulations. *Ecological*  
612 *Modelling*, 385, 173–181.
- 613 Cotter, C., Crisan, D., Holm, D., Pan, W., & Shevchenko, I. (2020). Modelling uncertainty  
614 using stochastic transport noise in a 2-layer quasi-geostrophic model. *Foundations of Data*  
615 *Science*, 2(2), 173.
- 616 Courtier, P., Andersson, E., Heckley, W., Vasiljevic, D., Hamrud, M., Hollingsworth, A., . . .  
617 Pailleux, J. (1998). The ecmwf implementation of three-dimensional variational assim-  
618 ilation (3d-var). i: Formulation. *Quarterly Journal of the Royal Meteorological Society*,  
619 124(550), 1783–1807.
- 620 Courtier, P., Thépaut, J.-N., & Hollingsworth, A. (1994). A strategy for operational im-  
621 plementation of 4d-var, using an incremental approach. *Quarterly Journal of the Royal*  
622 *Meteorological Society*, 120(519), 1367–1387.
- 623 Cramér, H. (1999). *Mathematical methods of statistics* (Vol. 9). Princeton university press.

- 624 Cuturi, M. (2013). Sinkhorn distances: Lightspeed computation of optimal transport. In  
625 *Advances in neural information processing systems* (pp. 2292–2300).
- 626 Cuturi, M., & Peyré, G. (2018). Semidual regularized optimal transport. *SIAM Review*,  
627 *60*(4), 941–965.
- 628 Dantzig, G. B., Orden, A., Wolfe, P., et al. (1955). The generalized simplex method for min-  
629 imizing a linear form under linear inequality restraints. *Pacific Journal of Mathematics*,  
630 *5*(2), 183–195.
- 631 Dee, D. P., & Da Silva, A. M. (1998). Data assimilation in the presence of forecast bias.  
632 *Quarterly Journal of the Royal Meteorological Society*, *124*(545), 269–295.
- 633 De Lannoy, G. J., Reichle, R. H., Houser, P. R., Pauwels, V., & Verhoest, N. E. (2007).  
634 Correcting for forecast bias in soil moisture assimilation with the ensemble kalman filter.  
635 *Water Resources Research*, *43*(9).
- 636 Dobrushin, R. L. (1970). Prescribing a system of random variables by conditional distribu-  
637 tions. *Theory of Probability & Its Applications*, *15*(3), 458–486.
- 638 Evensen, G. (1992). Using the extended kalman filter with a multilayer quasi-geostrophic  
639 ocean model. *Journal of Geophysical Research: Oceans*, *97*(C11), 17905–17924.
- 640 Evensen, G. (1994a). Sequential data assimilation with a nonlinear quasi-geostrophic model  
641 using Monte Carlo methods to forecast error statistics. *Journal of Geophysical Research*,  
642 *99*(C5), 10143. Retrieved from <http://doi.wiley.com/10.1029/94JC00572> doi: 10  
643 .1029/94JC00572
- 644 Evensen, G. (1994b). Sequential data assimilation with a nonlinear quasi-geostrophic model  
645 using monte carlo methods to forecast error statistics. *Journal of Geophysical Research:*  
646 *Oceans*, *99*(C5), 10143–10162.
- 647 Evensen, G. (2003). The ensemble kalman filter: Theoretical formulation and practical  
648 implementation. *Ocean dynamics*, *53*(4), 343–367.
- 649 Evensen, G., & Van Leeuwen, P. J. (1996). Assimilation of geosat altimeter data for the  
650 agulhas current using the ensemble kalman filter with a quasigeostrophic model. *Monthly*  
651 *Weather Review*, *124*(1), 85–96.
- 652 Feyeux, N., Vidard, A., & Nodet, M. (2018). Optimal transport for variational data assim-  
653 ilation. *Nonlinear Processes in Geophysics*, *25*(1), 55–66.
- 654 Fisher, M., & Gürol, S. (2017). Parallelization in the time dimension of four-dimensional vari-  
655 ational data assimilation. *Quarterly Journal of the Royal Meteorological Society*, *143*(703),  
656 1136–1147.
- 657 Fréchet, M. (1948). Les éléments aléatoires de nature quelconque dans un espace distancié.  
658 In *Annales de l'institut henri poincaré* (Vol. 10, pp. 215–310).

- 659 Gaspari, G., & Cohn, S. E. (1999). Construction of correlation functions in two and three  
660 dimensions. *Quarterly Journal of the Royal Meteorological Society*, 125(554), 723–757.
- 661 Gordon, N. J., Salmond, D. J., & Smith, A. F. (1993). Novel approach to nonlinear/non-  
662 gaussian bayesian state estimation. In *Iee proceedings f (radar and signal processing)*  
663 (Vol. 140, pp. 107–113).
- 664 Hamill, T. M. (2001). Interpretation of rank histograms for verifying ensemble forecasts.  
665 *Monthly Weather Review*, 129(3), 550–560.
- 666 Hamill, T. M., Whitaker, J. S., & Snyder, C. (2001). Distance-dependent filtering of back-  
667 ground error covariance estimates in an ensemble kalman filter. *Monthly Weather Review*,  
668 129(11), 2776–2790.
- 669 Hellinger, E. (1909). Neue begründung der theorie quadratischer formen von unendlichvie-  
670 len veränderlichen. *Journal für die reine und angewandte Mathematik (Crelles Journal)*,  
671 1909(136), 210–271.
- 672 Houtekamer, P. L., & Mitchell, H. L. (1998). Data assimilation using an ensemble kalman  
673 filter technique. *Monthly Weather Review*, 126(3), 796–811.
- 674 Houtekamer, P. L., & Mitchell, H. L. (2001). A sequential ensemble kalman filter for  
675 atmospheric data assimilation. *Monthly Weather Review*, 129(1), 123–137.
- 676 Houtekamer, P. L., & Zhang, F. (2016). Review of the ensemble kalman filter for atmospheric  
677 data assimilation. *Monthly Weather Review*, 144(12), 4489–4532.
- 678 Janjić, T., Nerger, L., Albertella, A., Schröter, J., & Skachko, S. (2011). On domain  
679 localization in ensemble-based kalman filter algorithms. *Monthly Weather Review*, 139(7),  
680 2046–2060.
- 681 Kalman, R. E. (1960). A New Approach to Linear Filtering and Prediction Problems.  
682 *Journal of Basic Engineering*. doi: 10.1115/1.3662552
- 683 Kalnay, E. (2003). *Atmospheric modeling, data assimilation and predictability*. Cambridge  
684 university press.
- 685 Kantorovich, L. V. (1942). On the translocation of masses. In *Dokl. akad. nauk. ussr (ns)*  
686 (Vol. 37, pp. 199–201).
- 687 Kapur, J. N. (1994). *Measures of information and their applications*. Wiley-Interscience.
- 688 Kolouri, S., Park, S. R., Thorpe, M., Slepcev, D., & Rohde, G. K. (2017). Optimal mass  
689 transport: Signal processing and machine-learning applications. *IEEE signal processing*  
690 *magazine*, 34(4), 43–59.
- 691 Kullback, S., & Leibler, R. A. (1951). On information and sufficiency. *The annals of*  
692 *mathematical statistics*, 22(1), 79–86.

- 693 Kutta, W. (1901). Beitrag zur naherungsweise integration totaler differentialgleichungen.  
694 *Z. Math. Phys.*, 46, 435–453.
- 695 Lei, L., Whitaker, J. S., & Bishop, C. (2018). Improving assimilation of radiance observa-  
696 tions by implementing model space localization in an ensemble kalman filter. *Journal of*  
697 *Advances in Modeling Earth Systems*, 10(12), 3221–3232.
- 698 Lguensat, R., Tandeo, P., Ailliot, P., Pulido, M., & Fablet, R. (2017). The analog data  
699 assimilation. *Monthly Weather Review*, 145(10), 4093–4107.
- 700 Li, L., Vidard, A., Le Dimet, F.-X., & Ma, J. (2018). Topological data assimilation using  
701 wasserstein distance. *Inverse Problems*, 35(1), 015006.
- 702 Li, R., Jan, N. M., Huang, B., & Prasad, V. (2019). Constrained ensemble kalman filter  
703 based on kullback–leibler divergence. *Journal of Process Control*, 81, 150–161.
- 704 Li, T., Bolic, M., & Djuric, P. M. (2015). Resampling methods for particle filtering: classifi-  
705 cation, implementation, and strategies. *IEEE Signal processing magazine*, 32(3), 70–86.
- 706 Li, Z., Zang, Z., Li, Q., Chao, Y., Chen, D., Ye, Z., . . . Liou, K. (2013). A three-dimensional  
707 variational data assimilation system for multiple aerosol species with wrf/chem and an  
708 application to pm 2.5 prediction. *Atmospheric Chemistry and Physics*, 13(8), 4265–4278.
- 709 Lin, L.-F., Ebtehaj, A. M., Flores, A. N., Bastola, S., & Bras, R. L. (2017). Combined  
710 assimilation of satellite precipitation and soil moisture: A case study using trmm and  
711 smos data. *Monthly Weather Review*, 145(12), 4997–5014.
- 712 Lorenc, A., Ballard, S., Bell, R., Ingleby, N., Andrews, P., Barker, D., . . . others (2000).  
713 The met. office global three-dimensional variational data assimilation scheme. *Quarterly*  
714 *Journal of the Royal Meteorological Society*, 126(570), 2991–3012.
- 715 Lorenc, A. C. (1986). Analysis methods for numerical weather prediction. *Quarterly Journal*  
716 *of the Royal Meteorological Society*, 112(474), 1177–1194.
- 717 Lorenz, E. N. (1995). Predictability-a problem partly solved. In *Predictability of weather and*  
718 *climate*. ECMWF. Retrieved from <https://www.ecmwf.int/node/10829> doi: 10.1017/  
719 CBO9780511617652.004
- 720 Lorenz, E. N., & Emanuel, K. A. (1998). Optimal sites for supplementary weather ob-  
721 servations: Simulation with a small model. *Journal of the Atmospheric Sciences*, 55(3),  
722 399–414.
- 723 Maclean, J., Santitissadeekorn, N., & Jones, C. K. (2017). A coherent structure approach for  
724 parameter estimation in lagrangian data assimilation. *Physica D: Nonlinear Phenomena*,  
725 360, 36–45.
- 726 McCann, R. J. (1997). A convexity principle for interacting gases. *Advances in mathematics*,  
727 128(1), 153–179.

- 728 Monge, G. (1781). Mémoire sur la théorie des déblais et des remblais. *Histoire de l'Académie*  
729 *Royale des Sciences de Paris*.
- 730 Nerger, L., Janjić, T., Schröter, J., & Hiller, W. (2012a). A regulated localization scheme  
731 for ensemble-based kalman filters. *Quarterly Journal of the Royal Meteorological Society*,  
732 *138*(664), 802–812.
- 733 Nerger, L., Janjić, T., Schröter, J., & Hiller, W. (2012b). A unification of ensemble square  
734 root kalman filters. *Monthly Weather Review*, *140*(7), 2335–2345.
- 735 Ning, L., Carli, F. P., Ebtehaj, A. M., Foufoula-Georgiou, E., & Georgiou, T. T. (2014).  
736 Coping with model error in variational data assimilation using optimal mass transport.  
737 *Water Resources Research*, *50*(7), 5817–5830.
- 738 Orlin, J. B. (1993). A faster strongly polynomial minimum cost flow algorithm. *Operations*  
739 *research*, *41*(2), 338–350.
- 740 Pass, B. (2015). Multi-marginal optimal transport: theory and applications. *ESAIM:*  
741 *Mathematical Modelling and Numerical Analysis*, *49*(6), 1771–1790.
- 742 Pedlosky, J., et al. (1987). *Geophysical fluid dynamics* (Vol. 710). Springer.
- 743 Penny, S., Bach, E., Bhargava, K., Chang, C.-C., Da, C., Sun, L., & Yoshida, T. (2019).  
744 Strongly coupled data assimilation in multiscale media: Experiments using a quasi-  
745 geostrophic coupled model. *Journal of Advances in Modeling Earth Systems*, *11*(6), 1803–  
746 1829.
- 747 Peyré, G., Cuturi, M., et al. (2019). Computational optimal transport. *Foundations and*  
748 *Trends in Machine Learning*, *11*(5-6), 355–607.
- 749 Pitt, M. K., & Shephard, N. (1999). Filtering via simulation: Auxiliary particle filters.  
750 *Journal of the American statistical association*, *94*(446), 590–599.
- 751 Poterjoy, J., & Anderson, J. L. (2016). Efficient assimilation of simulated observations in  
752 a high-dimensional geophysical system using a localized particle filter. *Monthly Weather*  
753 *Review*, *144*(5), 2007–2020.
- 754 Poterjoy, J., & Zhang, F. (2014). Intercomparison and coupling of ensemble and four-  
755 dimensional variational data assimilation methods for the analysis and forecasting of hur-  
756 ricane karl (2010). *Monthly Weather Review*, *142*(9), 3347–3364.
- 757 Pulido, M., & van Leeuwen, P. J. (2019). Sequential monte carlo with kernel embedded  
758 mappings: The mapping particle filter. *Journal of Computational Physics*, *396*, 400–415.
- 759 Rabier, F., Järvinen, H., Klinker, E., Mahfouf, J.-F., & Simmons, A. (2000). The ecmwf  
760 operational implementation of four-dimensional variational assimilation. i: Experimental  
761 results with simplified physics. *Quarterly Journal of the Royal Meteorological Society*,  
762 *126*(564), 1143–1170.

- 763 Rabin, J., Peyré, G., Delon, J., & Bernot, M. (2011). Wasserstein barycenter and its  
764 application to texture mixing. In *International conference on scale space and variational*  
765 *methods in computer vision* (pp. 435–446).
- 766 Rao, C. R., Rao, C. R., Statistiker, M., Rao, C. R., & Rao, C. R. (1973). *Linear statistical*  
767 *inference and its applications* (Vol. 2). Wiley New York.
- 768 Reich, S. (2013). A nonparametric ensemble transform method for bayesian inference. *SIAM*  
769 *Journal on Scientific Computing*, 35(4), A2013–A2024.
- 770 Reichle, R. H., McLaughlin, D. B., & Entekhabi, D. (2002). Hydrologic data assimilation  
771 with the ensemble kalman filter. *Monthly Weather Review*, 130(1), 103–114.
- 772 Runge, C. (1895). Über die numerische auflösung von differentialgleichungen. *Mathematische*  
773 *Annalen*, 46(2), 167–178.
- 774 Shen, Z., & Tang, Y. (2015). A modified ensemble kalman particle filter for non-gaussian  
775 systems with nonlinear measurement functions. *Journal of Advances in Modeling Earth*  
776 *Systems*, 7(1), 50–66.
- 777 Sinkhorn, R. (1967). Diagonal Equivalence to Matrices with Prescribed Row and Column  
778 Sums. *The American Mathematical Monthly*. doi: 10.2307/2314570
- 779 Spiller, E. T., Budhiraja, A., Ide, K., & Jones, C. K. (2008). Modified particle filter  
780 methods for assimilating lagrangian data into a point-vortex model. *Physica D: Nonlinear*  
781 *Phenomena*, 237(10-12), 1498–1506.
- 782 Srivastava, S., Li, C., & Dunson, D. B. (2018). Scalable bayes via barycenter in wasserstein  
783 space. *The Journal of Machine Learning Research*, 19(1), 312–346.
- 784 Tagade, P., & Ravela, S. (2014). On a quadratic information measure for data assimilation.  
785 In *2014 american control conference* (pp. 598–603).
- 786 Tamang, S. K., Ebtehaj, A., Van Leeuwen, P. J., Zou, D., & Lerman, G. (2021). En-  
787 semble riemannian data assimilation over the wasserstein space. *Nonlinear Processes in*  
788 *Geophysics Discussions*, 1–26.
- 789 Tamang, S. K., Ebtehaj, A., Zou, D., & Lerman, G. (2020). Regularized variational data  
790 assimilation for bias treatment using the wasserstein metric. *Quarterly Journal of the*  
791 *Royal Meteorological Society*.
- 792 Tang, Y., Deng, Z., Manoj, K., & Chen, D. (2014). A practical scheme of the sigma-  
793 point kalman filter for high-dimensional systems. *Journal of Advances in Modeling Earth*  
794 *Systems*, 6(1), 21–37.
- 795 Tian, X., Zhang, H., Feng, X., & Xie, Y. (2018). Nonlinear least squares en4dvar to 4denvar  
796 methods for data assimilation: Formulation, analysis, and preliminary evaluation. *Monthly*  
797 *Weather Review*, 146(1), 77–93.

- 798 Tippett, M. K., Anderson, J. L., Bishop, C. H., Hamill, T. M., & Whitaker, J. S. (2003).  
799 Ensemble square root filters. *Monthly Weather Review*, *131*(7), 1485–1490.
- 800 Trevisan, A., & Palatella, L. (2011). On the kalman filter error covariance collapse into the  
801 unstable subspace. *Nonlinear Processes in Geophysics*, *18*(2), 243.
- 802 Van Leeuwen, P. J. (2009). Particle filtering in geophysical systems. *Monthly Weather*  
803 *Review*, *137*(12), 4089–4114.
- 804 van Leeuwen, P. J. (2010). Nonlinear data assimilation in geosciences: an extremely efficient  
805 particle filter. *Quarterly Journal of the Royal Meteorological Society*, *136*(653), 1991–  
806 1999.
- 807 Van Leeuwen, P. J. (2020). A consistent interpretation of the stochastic version of the  
808 ensemble kalman filter. *Quarterly Journal of the Royal Meteorological Society*, *146*(731),  
809 2815–2825.
- 810 Villani, C. (2003). *Topics in Optimal Transportation*. doi: 10.1090/gsm/058
- 811 Villani, C. (2008). *Optimal transport: old and new* (Vol. 338). Springer Science & Business  
812 Media.
- 813 Vissio, G., Lembo, V., Lucarini, V., & Ghil, M. (2020). Evaluating the performance of  
814 climate models based on wasserstein distance. *Geophysical Research Letters*, *47*(21),  
815 e2020GL089385.
- 816 Yang, Y., & Engquist, B. (2018). Analysis of optimal transport and related misfit functions  
817 in full-waveform inversion. *Geophysics*, *83*(1), A7–A12.
- 818 Yang, Y., Engquist, B., Sun, J., & Hamfeldt, B. F. (2018). Application of optimal transport  
819 and the quadratic wasserstein metric to full-waveform inversion. *Geophysics*, *83*(1), R43–  
820 R62.
- 821 Yong, P., Huang, J., Li, Z., Liao, W., & Qu, L. (2019). Least-squares reverse time migration  
822 via linearized waveform inversion using a wasserstein metric. *Geophysics*, *84*(5), S411–  
823 S423.
- 824 Zupanski, M. (1993). Regional 4-Dimensional Variational Data Assimilation in a Quasi-  
825 Operational Forecasting Environment. *Monthly Weather Review*, *121*(8), 2396–2408.